TFvelo: gene regulation inspired RNA velocity estimation

Jiachen Li[1], Xiaoyong Pan[1], Ye Yuan[1]*, Hong-Bin Shen[1]*
[1]Institute of Image Processing and Pattern Recognition, Shanghai Jiao Tong University, and Key Laboratory of System Control and Information Processing, Ministry of Education of China, Shanghai, 200240, China
*Address correspondence to Y.Y at: yuanye_auto@sjtu.edu.cn, H.B. Shen at: hbshen@sjtu.edu.cn

Abstract

RNA velocity is closely related with cell fate and is an important indicator for the prediction of cell states with elegant physical explanation derived from single-cell RNA-seq data. Most existing RNA velocity models aim to extract dynamics from the phase delay between unspliced and spliced mRNA for each individual gene. However, unspliced/spliced mRNA abundance may not provide sufficient signal for dynamic modeling, or it may even be absent in some datasets (e.g., fluorescence *in situ* hybridization data). Consequently, the dynamics constructed by previous RNA velocity methods may not fit the unspliced/spliced data well, especially in phase portraits. Motivated by the finding that RNA velocity could be driven by the transcriptional regulation, we propose TFvelo, which expands RNA velocity concept to various single-cell datasets without splicing information, by introducing gene regulatory network information. Our experiments on synthetic data, scRNA-Seq and MERFISH data demonstrate that TFvelo can accurately fit genes dynamics on phase portraits, and effectively infer cell pseudo-time and trajectory from RNA abundance data. TFvelo opens a novel, robust and accurate avenue for modeling RNA velocity for single cell data.

Introduction

Single-cell RNA sequencing (scRNA-seq)[1-3] provides a wealth of information about the gene expression profile of individual cells. To expand the scope of scRNA-seq analysis beyond a static snapshot and capture cellular dynamics without tracking alive individual cells over time, many pseudotime and trajectory inference (TI) approaches, like PAGA[4], Monocle[5], Slingshot[6] and Palantir[7] have been developed. In recent years, RNA velocity[8] theory was proposed, which describes the time derivative of gene abundance in a physical-informed approach, by modeling the relationship between the unspliced (immature) and spliced (mature) mRNAs. Combining velocities across multiple genes, velocity-based pseudotime and cell fate can be inferred from the transition probability between cells. To estimate the RNA velocity, velocyto[8] is introduced as the vanilla approach with a steady state assumption. ScVelo[9] models the dynamics without the steady state assumption and employs an Expectation-Maximization (EM) approach for

better reconstructing the underlying kinetics.

More recently, several approaches have been developed to improve the estimation of RNA velocity. For instance, VeloAE[10] utilized an auto-encoder and low-dimensional space to smooth RNA velocity. Still in the unspliced/spliced space, DeepCycle[11] used an autoencoder to map cell cycle-related genes. UniTVelo[12] directly designed a function of time to model the spliced RNA level. In contrast to deterministic models, VeloVI[13], Pyrovelocity[14] and veloVAE[15] estimated RNA velocity using Bayesian inference frameworks. LatentVelo[16] embeds the unspliced and spliced expression into the latent space with a variational auto-encoder, so that a low-dimensional representation of RNA velocity could be obtained. CellDancer[17] models the transcription, splicing and degradation rate of a gene as a function of its unspliced and spliced counts with a neural network. Furthermore, apart from the unspliced/spliced data, dynamics can also be modeled with additional information. For instance, Dynamo[18] improve the RNA velocity model by using the new/total labeled RNA-seq[19]. Taking the advantage of single-cell multi-omics technology[20,21] , RNA velocity analysis can be expanded to protein abundances (protaccel[22]) and single-cell ATAC-seq (MultiVelo[23]) datasets. However, these additional omics data or labeling may be cost or even not available in most single cell datasets.

While RNA velocity theory has improved the inference of single-cell trajectories, pseudo-time, and gene regulation inference in numerous studies[24], current RNA velocity models still face severe challenges. Firstly, RNA velocity models always treat each gene independently and do not take the underlying regulation into consideration[25], although it is expected to be helpful for cell fate inference by integrating gene regulatory mechanism analysis. Secondly, these models can not fit the gene dynamics well on most genes, which might be because that the transcriptional dynamics of mRNA splicing may not provide sufficient signal in single cell resolution[25]. The high sparsity and noise nature of unspliced mRNA counts[26,27] could be one significant reason. Most conventional approaches assume that the joint plot between unspliced and spliced expression should form a clockwise curve on the phase portrait[8,9,12] because of the phase delay within them, which is, nevertheless, rarely observed from the data. Last but not least, the RNA velocity models can only be applied to scRNA-seq datasets with unspliced/spliced or new/total labels. However, the abundance of unspliced/spliced data may not be available in certain datasets, such as those obtained through Fluorescence *In Situ* Hybridization (FISH) technologies[28], and some human sequencing data due to privacy restrictions. These challenges motivate us to construct the gene dynamics based on regulation, instead of only relying on the unspliced/spliced counts.

The gene regulation has been explored a lot in the field of single cell research[29-33]. In this study, we aim at inferring the gene dynamics and cell fate based on the underlying regulatory among genes. To this end, we investigate the relationship between gene regulatory patterns and RNA velocity, which reveals that the RNA velocity can be approximately estimated as a linear combination of the expression levels of

transcription factors (TFs). Notably, the TFs with the non-zero weights are significantly enriched with TF set functionally linked to the target gene. In addition, we find that the joint distribution of expressions between a TF and its target could form a clockwise curve on the co-expression plot[34], indicating the phase delay between them. Those findings imply that the abundance of TFs could also be used to construct dynamics model of RNA velocity.

Here we propose a new RNA velocity estimation method, TFvelo, to address the challenges mentioned above. TFvelo is a novel method that models the RNA velocity, which means the time derivative of the expression level here, based on the expression levels of TFs. The computational framework of TFvelo relies on a generalized EM algorithm, which iteratively updates the learned representation of TFs, the latent time of cells, and the parameters in the dynamic equation. Compared with those TI methods, TFvelo is a velocity-based pseudotime inferenced method that does not require the initial cell state annotation, and offers additional analysis capabilities, such as modeling the dynamics of each gene, identifying best fitted genes and significant TFs. As a result, this approach enables RNA velocity modeling to be robustly applied on those genes where unspliced count is sparse, and even those datasets without splicing information. Finally, using both synthetic data and real datasets, we demonstrate that the TFvelo model can capture the dynamics on phase portraits of TFs-target, accurately infer the pseudo-time and the developmental trajectories of cells and help explore biological findings.

Results

Findings: RNA velocity can be approximately estimated with TFs' abundance.
The fact that RNA velocity can be modelled by the transcriptional regulation is supported by the following two findings. We find that the RNA velocity model by previous approach can be approximately estimated as a linear combination of TFs' abundance. On the scRNA-Seq pancreas dataset[8], given a target gene, Least Absolute Shrinkage and Selection Operator (LASSO) regression is applied to predict RNA velocity modelled by scVelo, based on the expression level of TFs and the target gene itself (**Fig. S1a**). Here we run scVelo pipeline on pancreas dataset with the default parameters to get the velocities, and only apply LASSO regression to those genes which are modelled by scVelo. We feed all TFs[35] into LASSO, and get a sparse weights-vector where only some TFs have non-zero weights. As a result, the RNA velocity of gene g can be estimated as:

$$v_g = \sum_{TF_i \in S_g} w_{g,TF_i} e_{TF_i} + w_{g,g} e_g \tag{1}$$

where S_g represents the set of TFs, e_{TF_i} and e_g are the expression level of TF_i and

gene g respectively, w_{g,TF_i} and $w_{g,g}$ are the weights of TF_i and the target gene itself.

Cells are separated into training and test sets to evaluate the LASSO model. The regression results on the test set shows a high correlation between the predicted and labeled velocity, as demonstrated in **Fig. S1 b-e**, which indicates that velocity of the target gene can be predicted based on the expressions of its TFs. In addition, as shown in **Table S1**, the TFs with non-zero positive weights are significantly enriched in TFs set functionally linked to the target gene (according to ENCODE TF-target datasets [36]) with p value of 6.66e-06 (one-sided t-test), further suggesting that velocity could be modelled by TFs. Secondly, due to regulatory relationship between TF and target, the expression levels of them change asynchronously, which could result in a clockwise curve on the phase portraits. And as expected, we find the desired clockwise curve on the co-expression plots between some TF-target pairs[34] (**Fig. S2**), which is similar to the theoretical prediction of existing velocity models on unspliced-spliced space. These findings suggest that it is possible to construct a novel RNA velocity model based on the expression of TFs, instead of using unspliced/spliced RNA counts or any additional experimental omics data and labels.

Estimate RNA velocity with TFvelo

Here we report TFvelo to estimate the RNA velocity of a target gene using the abundance of the target gene itself and its potential TFs. **Fig. 1a** provides an example of phase portrait fitting on a gene from pancreas dataset, to explain how TFvelo outperforms splicing-based methods. Previous methods focus on modeling the dynamics between the spliced and unspliced RNAs, while transcriptional dynamics of RNA splicing may not provide sufficient signal[25], and the 2D unspliced-spliced RNA level could be too noisy or sparse to fit. By comparison, TFvelo considers the relationship between the target gene and multiple TFs, by learning a representation of regulation, allowing for more robust and accurate modeling based on gene regulatory network.

For a target gene g, TFvelo explores the relationships between its expression level y_g and the regulation of TFs on g. In TFvelo, the RNA velocity $\frac{dy_g(t)}{dt}$, which is defined as the time derivative of RNA abundance, is determined by the abundance of involved TFs $\boldsymbol{X_g}$ and itself,

$$\frac{dy_g(t)}{dt} = h\big(\boldsymbol{X_g}(t); \Psi_g\big). \tag{2}$$

Using a top-down strategy, which can relax the gene dynamics to more flexible profiles[12], TFvelo directly designs a profile function of target gene's expression level,

$$y_g(t) = f(t; \Phi_g). \quad (3)$$

where Ψ_g and Φ_g are two sets of gene-specific time-invariant parameters, which describe the influence of TFs on the target gene, and the shape of phase portraits, respectively. Considering that linear models have been employed to represent the gene regulatory in previous studies[37-39], $h(\boldsymbol{X_g}(t), y_g(t); \Psi_g)$ is implemented with a linear model $\frac{dy_g(t)}{dt} = \boldsymbol{W_g}\boldsymbol{X_g}(t) - \gamma_g y_g(t)$. The profile function of $y_g(t)$ can be chosen flexibly from a series of second-order differentiable functions[12], which is designed as a sine function in implementation (**Methods**). This is because sine functions can model the nonmonotonic dynamics start from both down-regulation and up-regulation, which is not feasible for those methods relying on one switching time point[8,9,18].

For optimization, all learnable parameters are divided into three groups, which are cell-specific latent time t, TFs' weights $\boldsymbol{W_g}$ and the shape parameters of phase portraits Ψ_g, in which n_{cell} and n_{TF} represent number of cells and number of genes, respectively. A generalized EM[40,41] algorithm is adopted to minimize the loss function in each iteration, by updating the three groups of parameters alternately (**Fig. 1 f-h**). Based on the optimized models on all genes, we can obtain a transition matrix and calculate the pseudotime and velocity stream for cell trajectory analysis. Please find the details in **Methods**.

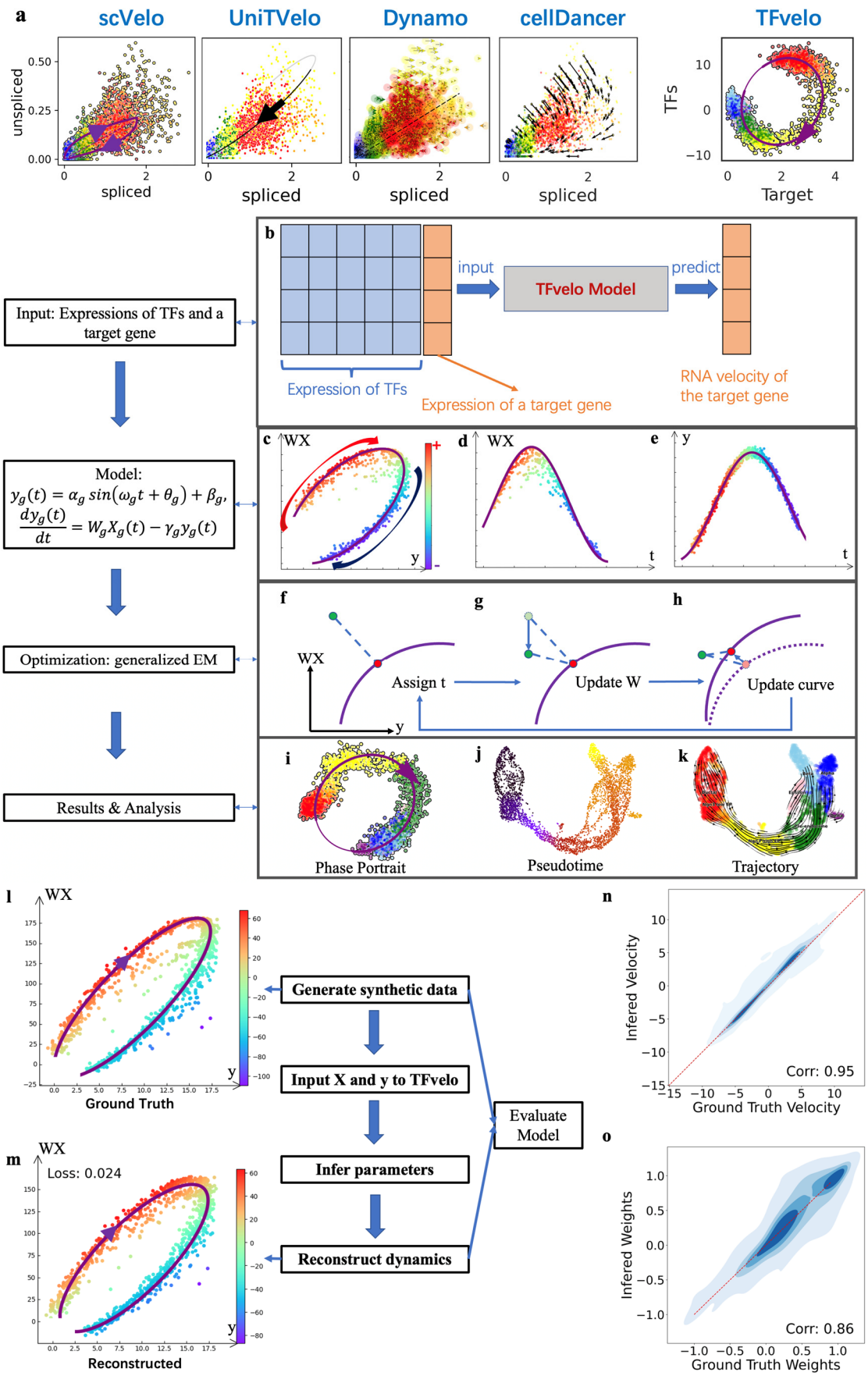
a
scVelo
UniTVelo
Dynamo
cellDancer
TFvelo
unspliced
spliced
TFs
Target
b
input
TFvelo Model
predict
Expression of TFs
Expression of a target gene
RNA velocity of the target gene
Input: Expressions of TFs and a target gene
Model:
$y_g(t) = \alpha_g \sin(\omega_g t + \theta_g) + \beta_g$,
$\frac{dy_g(t)}{dt} = W_g X_g(t) - \gamma_g y_g(t)$
Optimization: generalized EM
Results & Analysis
c
d
e
WX
y
t
f
g
h
Assign t
Update W
Update curve
i
j
k
Phase Portrait
Pseudotime
Trajectory
l
Ground Truth
m
Loss: 0.024
Reconstructed
Generate synthetic data
Input X and y to TFvelo
Infer parameters
Reconstruct dynamics
Evaluate Model
n
Infered Velocity
Ground Truth Velocity
Corr: 0.95
o
Infered Weights
Ground Truth Weights
Corr: 0.86

Figure 1. The overview of TFvelo. (a) The comparison among constructed dynamics on LITAF gene in Pancreas dataset by TFvelo and previous approaches. Cells are colored in the same way as those in **Fig. 2a**. (b) The workflow of TFvelo. (c-e) The phase portrait plot on WX-y space, the plot of WX with respect to pseudotime, and the plot of y with respect to pseudotime. The color bar indicating the RNA velocity is share by the three panels. For simplification, W_g, X_g, y_g and t_g, are written as $\mathrm{W}, \mathrm{X}, \mathrm{y}$ and t, respectively. (f-h) The steps within each iteration of the generalized EM algorithm. Here the purple line represents the current prediction by the model. (f) Assignment of latent time to each cell (in green) to find the corresponding target point (shown in red), which is the nearest point to the cell on the purple line. (g) Optimization of the weights W to move all cells along the WX axis, minimizing the mean loss over all cells. (h) Optimization of the parameters in the dynamical function, to move the target point on the curve closer to each cell. (i-k) Visualization and analysis of TFvelo's results, including phase portrait fitting pseudo-time inference, and cell trajectory prediction. (l-o) Simulation on synthetic dataset. (l) An example of the generated synthetic dynamics. (m) Reconstructed dynamics by TFvelo of the sample shown in (l) with MSE loss. (n) The joint plot of ground truth velocity and inferred velocity with their spearman correlation. The red reference line refers to that the ground truth is equal to the inferred value. (o) The joint plot of ground truth weights and inferred weights with their spearman correlation.

TFvelo can reconstruct the dynamic model and detect the regulation relationship on synthetic datasets.

To validate that TFvelo can detect the underlying dynamic from data, we firstly test it on a synthetic dataset (see **Methods**), where a target gene is regulated by 10 TFs, and the corresponding weights are either positive or negative, representing that TF may up-regulate or down-regulate the target gene, respectively. We randomly generate 200 synthetic gene dynamics on 1000 cells with different ground truth parameters. For each of them, the TFvelo reconstructs the dynamic function and estimates the weight of each TF, based on the simulated expressions of TFs and target.

The performance of TFvelo was evaluated using the spearman correlation between the ground truth and the reconstructed values. Under 20 iterations for optimization, the spearman correlation coefficient between the ground truth weights and inferred weights of TFs is 0.86, and that for velocity estimation is 0.95 (**Fig. 1n&o**). The high consistence shows that TFvelo can effectively reconstruct the underlying dynamics. In addition, the high F1 score (0.951) and high ratio of area under the receiver operating characteristic (ROC) curve (0.968) also demonstrate that TFvelo can correctly recognize whether the weight is positive or negative. Please see **Supplementary Information Section 3** for details on the synthetic dataset.

TFvelo can model cell differentiation process on Pancreas dataset.

To evaluate TFvelo on real scRNA-seq data, we first apply it to the dataset of E15.5

mouse pancreas[8], which has been widely adopted in previous RNA velocity studies. The pseudo-time and trajectory predicted by TFvelo can identify the differentiation process (**Fig. 2a&b**). Compared with previous methods, TFvelo shows advantage on phase portrait fitting. Example genes are shown in **Fig. 2c** and **Fig. S7**. **Fig. 2c** compares the phase portrait fitting of different methods, and **Fig. S7** provides the gene expression dynamics resolved along gene-specific latent time obtained by scVelo and TFvelo. The expression of H19, which plays an important role in early development[42], is found to increase at the beginning and then decrease at the stage of Ngn3 high EP by TFvelo. For MAML3, only TFvelo can correctly detect the process that starts with up-regulation then turns to down-regulation. Other methods can not correctly detect the order between pre-endocrine cells (in green) and those endocrine populations, including alpha, beta, delta and epsilon cells (in blue, light blue, purple and pink).

To quantitatively evaluate the phase portrait fitting, we propose three metrics, including: (1) The intra-class distance on phase portrait, which reflects how cells within the same type gather on the phase portrait (the lower the better). (2) The inter-class distance on phase portrait, which reflects how cells from different types are separated well on the phase portrait (the higher the better). (3) The fitting error on phase portrait, which measures the normalized distance between each cell to the constructed model on the phase portrait. We calculate these metrics based on the genes that can be commonly modeled by all methods. For the “intra-class distance” and “inter class distance”, we take the Paired Samples T Test between the value obtained on the same gene by TFvelo’s phase portrait and the un/spliced phase portrait, which is commonly adopted by all baselines. The TFvelo results (**Fig. 2d-f**) show advantage with extreme high significance (p=4.23e-51 and p=5.65e-117). Apart from the noise and high sparsity (**Fig. S6**) in splicing data, considering that the splicing can be accomplished within 30 seconds[43], the too short phase delay between the unspliced and spliced mRNA might also give the phase portrait fitting more challenge (**Fig. S12**). Compared with those un/spliced based approaches, TFvelo can achieve lower intra-class distance, higher inter-class distance and lower fitting error. To draw a conclusion, TFvelo can address the current issue caused by noisy un/spliced data for RNA velocity modeling, by using the learned feature with transcription regulation.

In addition, we also employed two metrics adopted in VeloAE and UniTVelo, which are "Cross Boundary Direction Correctness (CBDir)” and "In Cluster Coherence (ICCoh)". CBDir assesses the correctness of transitions from one cell type to the next, utilizing boundary cells with ground truth annotations. ICCoh is computed using cosine similarity among cells within the same cluster, measuring the smoothness of velocity in high-dimensional space within clusters. As shown in **Fig. 2g&h**, TFvelo achieves similar median value compared to UniTVelo, and significantly outperforms the other methods. Also TFvelo can even achieve a high velocity confidence (**Fig. 2i**), which indicates a higher consistency of RNA velocities across neighboring cells in the UMAP space[9].

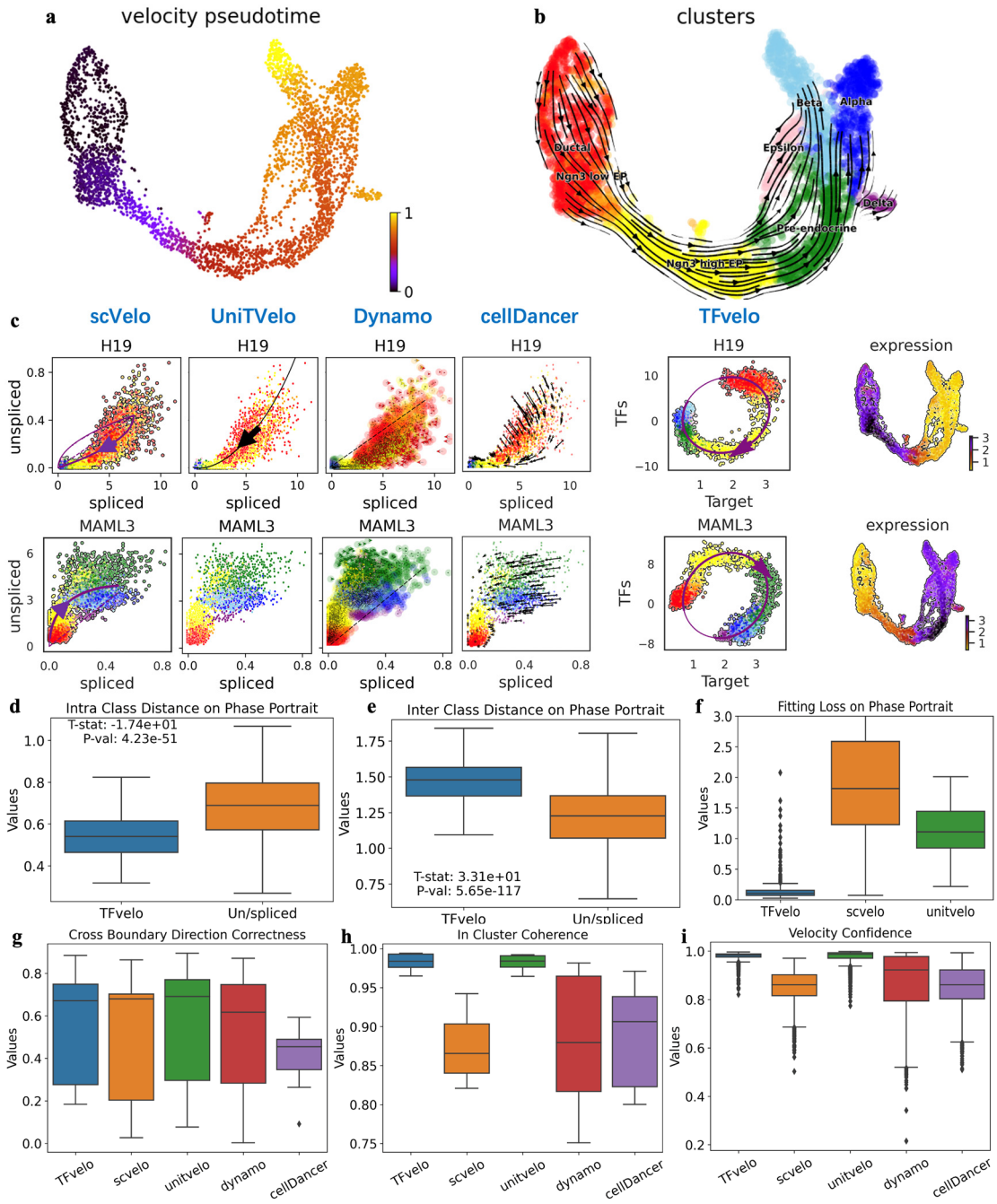

Figure 2. Results of TFvelo on pancreas dataset. (a) Pseudo-time inferred by TFvelo in the UMAP-based embedding space. (b) The stream plot projected to UMAP. The Ngn3 low/high EP denotes the neurogenin3 low/high epithelial cells. (c) Two example genes for illustrating the dynamics fitting in phase portrait. The cells are colored in the same way as panel (b). (d-f) The quantitative comparisons in phase portrait fitting. (d) Intra class distance. (e) Inter class distance. (f) Fitting loss. (g-h) The quantitative comparisons in high-dimensional space. (g) Cross boundary direction correctness. (h) In cluster coherence. (i) Velocity confidence. For each box-plot, the down, central and up hinges correspond to the first quartile, median value and third quartile, respectively. The whiskers extend to 1.5× the interquartile range of the distribution from the hinge. Data beyond the end of the whiskers are determined to be outliers and plotted

individually as diamonds.

Then we conduct KEGG pathways enrichment analysis based on the best fitted genes, and observe a strong enrichment associated with insulin secretion and the glucagon signaling pathway (**Fig. 3a**). Additionally, we find that REST and HMGN3 consistently exhibit high absolute weights on modeling most target genes (**Fig. 3b**). When examining the UMAP distribution, it is clear that REST expression decreases during differentiation, while HMGN3 expression increases (**Fig. 3c**). Previous research has established REST as a key negative regulator of endocrine differentiation during pancreas organogenesis[44,45]. Earlier studies have also report HMGN3 to be a regulator for insulin secretion in pancreatic cells [45]. We further analyze the weights of these two TFs on modeling genes within the insulin secretion pathway. REST consistently has a negative weight, while HMGN3 consistently exhibits a positive weight (**Fig. 3d**), which is consistent with the previous findings.

The comparison of phase between TFs and target are shown in **Fig. 3e**, which shows clear phase delay between the learned representation of TFs (WX) and target gene's expression. We also analyze the phase delay between a TF and the individual target. Among the two genes, HMGN3 has a positive weight on modeling SURF, where a phase delay between them can be observed. On the contrary, REST has a negative one on modeling ECE1, where their changing shows negative correlation.

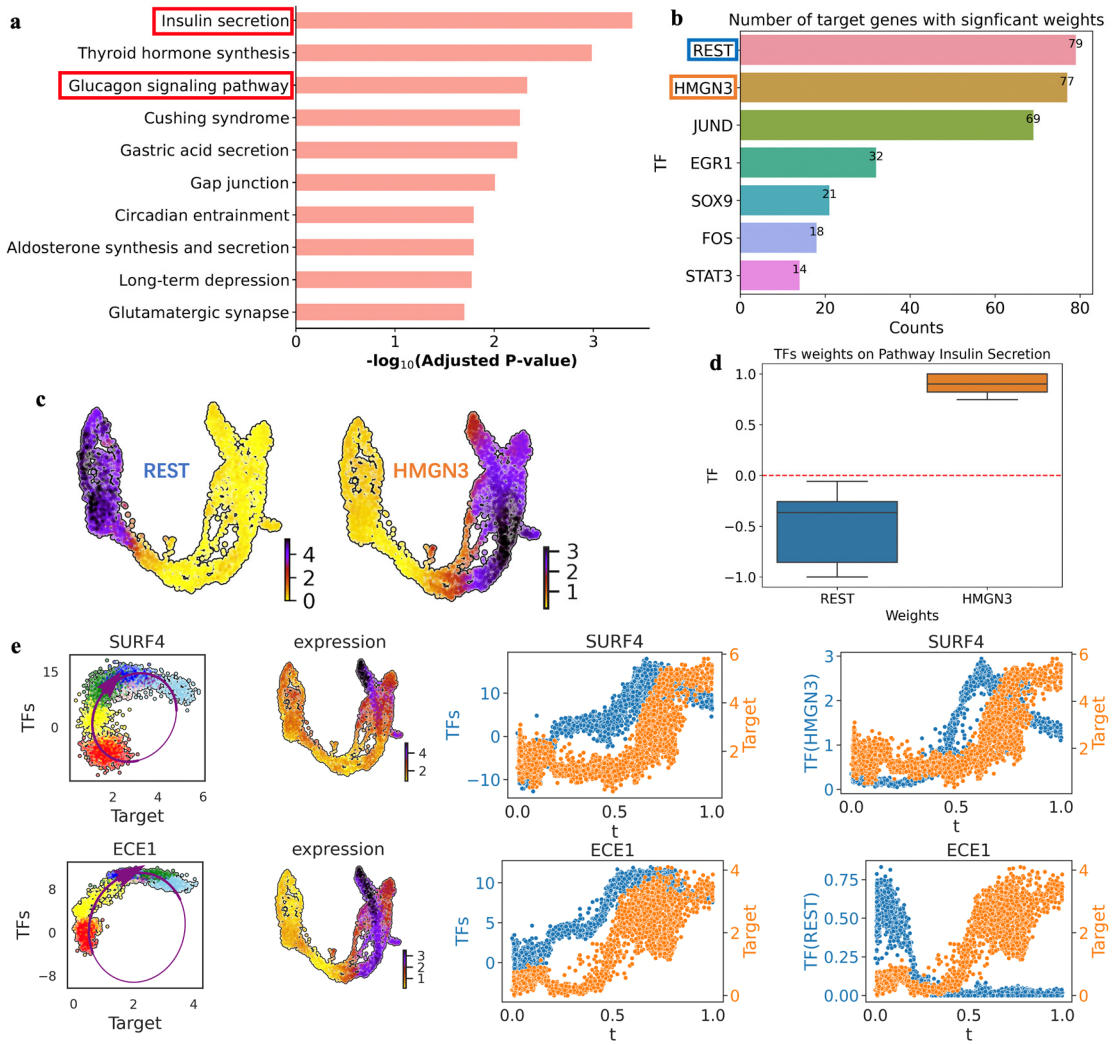

Figure 3. Biological analysis based on the results of TFvelo on pancreas dataset. (a) The KEGG pathway enrichment from the genes best fitted by TFvelo on pancreas dataset. (b) List of TFs having high weights on multiple target genes. The counts mean the number of target genes where the TF have a normalized weight whose absolute value is larger than 0.5. (c) The distribution of REST and HMGN3 on UMAP. (d) The weights distribution of TFs REST and HMGN3 on modeling in the genes that in the insulin secretion pathway. The down, central and up hinges correspond to the first quartile, median value and third quartile, respectively. The whiskers extend to 1.5× the interquartile range of the distribution from the hinge. (e) Phase analysis on two example genes. On each row, from the left to the right: the phase portrait fitting, the distribution of abundance on UMAP, the value of learned TFs representation (WX) and the target gene along with pseudotime, and the abundance of a TF and the target gene along with pseudotime.

TFvelo can model cell differentiation process on gastrulation erythroid dataset. The Gastrulation Erythroid dataset is selected from the transcriptional profile for mouse embryos[46], and has be adopted in RNA velocity studies[12]. Using TFvelo, the pseudo-time and cell development flow visualized by streamlines are consistent with the

325 development in the erythroid lineage, from blood progenitors to erythroid cells (**Figs.**
326 **4a** and **4b**). By comparison, several of the previous approaches cannot capture such
327 developmental dynamics, as shown in **Fig. 4d**.
328 The sparsity in data is a common challenge for scRNA-seq studies. Considering that
329 only about 20% of reads contained unspliced intronic sequences [8], the sparse unspliced
330 abundance is a large obstacle for dynamics fitting in phase portrait. Our quantitative
331 analysis of the sparsity in unspliced, spliced and total mRNA counts is shown in **Fig.**
332 **4c**, which verifies the high sparsity in unspliced counts. **Fig. 4e** shows the comparison
333 on two genes with very sparse unspliced counts to illustrate the advantage of TFvelo
334 for addressing the issue of sparsity. Although these genes can pass the filtering and
335 selection during preprocessing, they are still too sparse to provide sufficient information
336 for fitting the spiced-based models well. **Fig. 4f** provides more example genes of the
337 comparison between TFvelo and baselines. TACC1 is annotated as a gene involved in
338 promoting cell division prior to the formation of differentiated tissues[47]. In our
339 experiment, the expression of TACC1 initially increases, reaching its highest value in
340 blood progenitors 2, which is just before differentiation into erythroid cells.
341 Subsequently, TACC1's expression decreases with pseudo-time from erythroid cells 1
342 to erythroid cells 3. By comparison, previous approaches fail to detect a dynamic
343 starting from blood progenitors 1 (in red). As for HSP90AB1, only TFvelo can capture
344 the correct dynamics from the learned phase portrait.
345 We next take the GO term enrichment analysis based on the best fitted genes, and find
346 that the most significant GO terms include porphyrin-containing compound
347 biosynthetic process (GO:0006779) and heme biosynthetic process (GO:0006783),
348 which are directly related to erythroid development (**Fig. 4g**). In addition, the TFs
349 having high weights on most target genes are GATA1, GATA2 and LMO2 (**Fig. 4h**), all
350 of which has been reported to be involved in erythroid differentiation. GATA1 plays a
351 significant role in regulating the transcriptional aspects of erythroid maturation and
352 function[48]. GATA2 is verified to regulates hematopoietic stem cell proliferation and
353 differentiation[49]. LMO2 is a bridging molecule assembling an erythroid, DNA-binding
354 complex[50]. These findings demonstrate the potential of TFvelo in detecting important
355 regulatory genes from single cell data.

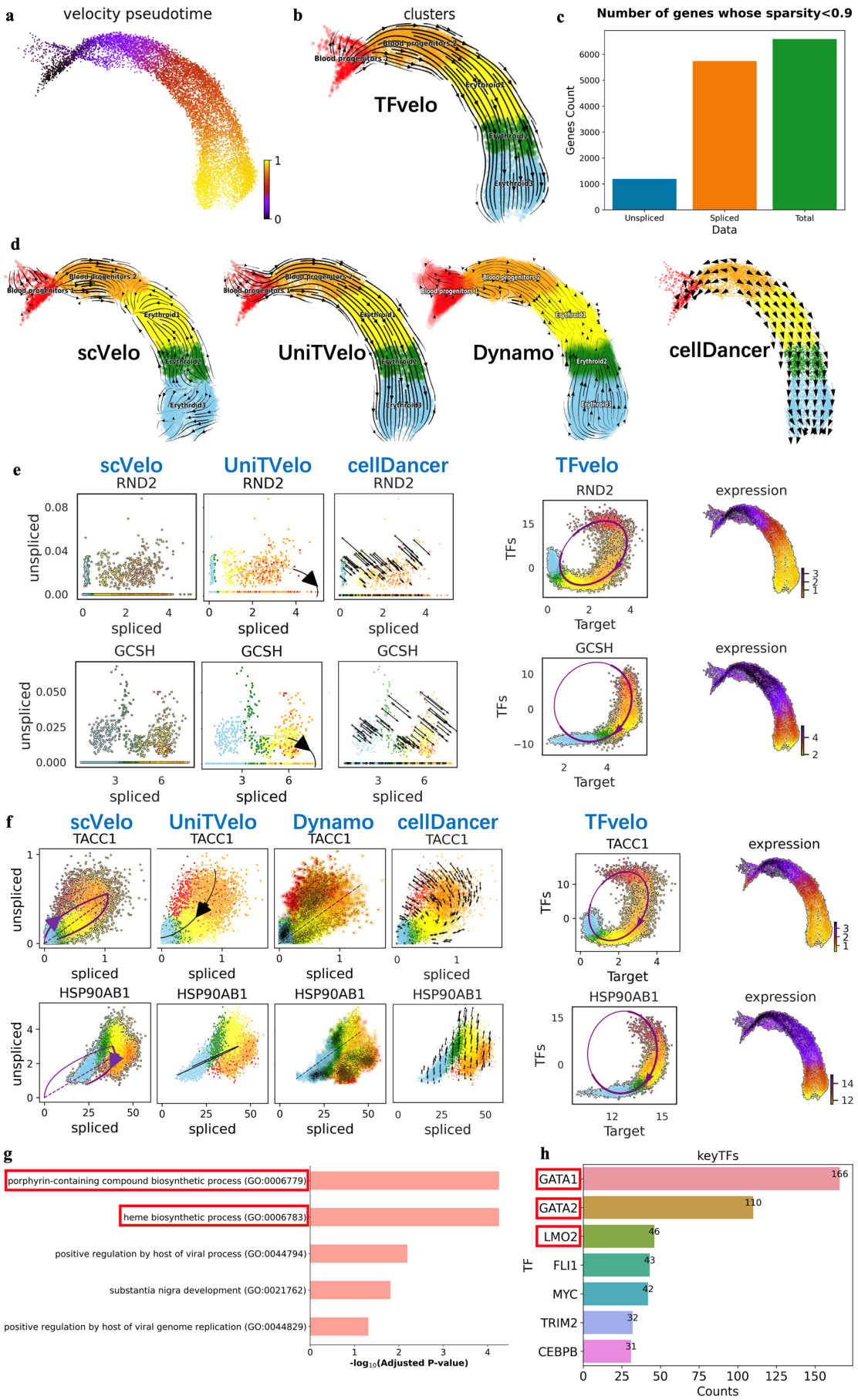
a
velocity pseudotime
b
clusters
TFvelo
c
Number of genes whose sparsity<0.9
Genes Count
Unspliced
Spliced
Total
Data
d
scVelo
UniTVelo
Dynamo
cellDancer
e
scVelo
UniTVelo
cellDancer
TFvelo
RND2
GCSH
unspliced
spliced
TFs
Target
expression
f
scVelo
UniTVelo
Dynamo
cellDancer
TFvelo
TACC1
HSP90AB1
g
porphyrin-containing compound biosynthetic process (GO:0006779)
heme biosynthetic process (GO:0006783)
positive regulation by host of viral process (GO:0044794)
substantia nigra development (GO:0021762)
positive regulation by host of viral genome replication (GO:0044829)
-log10(Adjusted P-value)
h
keyTFs
GATA1
GATA2
LMO2
FLI1
MYC
TRIM2
CEBPB
TF
Counts

Figure 4. Results of TFvelo on gastrulation erythroid dataset. (a) Pseudo-time inferenced by TFvelo projected into a UMAP-based embedding. (b) The stream plot obtained by TFvelo. (c) The sparsity for unspliced, spliced and total mRNA counts. The sparsity of a gene is defined as: $\text{Sparsity} = \frac{\text{The number of cells that the count of this gene is zero}}{\text{The total number of cells}}$. (d) The stream plot obtained by baseline approaches. (e) The phase portrait fitting on genes with sparse unspliced counts. (f) The phase portrait fitting on TACC1 and HSP90AB1 with sparse unspliced counts. (g) The GO term biological process enrichment based on the best fitted genes. (h) The number of target genes where the absolute value of the weight larger than 0.5 for each TF.

TFvelo can achieve competitive performance compared to Multivelo using only scRNA-seq data.

Next we apply TFvelo to a 10x multi-omics embryonic mouse brain dataset, where both Assay for Transposase-Accessible Chromatin with sequencing (ATAC-Seq)[51] and scRNA-seq are available. This dataset was employed in Multivelo study, which is an RNA velocity model designed for multi-omics datasets, capturing dynamics between chromatin accessibility and unspliced mRNA[23]. On this dataset, as described in the Multivelo study, Radial glia (RG) cells in the outer subventricular zone can generate neurons, astrocytes, and oligodendrocytes. The development of cortical layers follows an inside-out pattern during neuronal migration, with younger cells ascending to upper layers while older cells remain in deeper layers. RG cells can divide, producing intermediate progenitor cells (IPC) that act as neural stem cells and give rise to various mature excitatory neurons in cortical layers.

The pseudotime inferred by TFvelo closely resemble Multivelo's results (**Fig. 5a** and **b**), and both methods correctly identify the differentiation direction in most cells. Notably, TFvelo achieves this performance without using ATAC-seq data. **Fig. 5c** shows the phase portrait fitting of both methods, where Multivelo could show an additional c-u phase portrait, reflecting the joint plot between ATAC-seq and unspliced mRNA.

Regarding the AHI1 gene, Multivelo mistakenly constructs a cyclic dynamic, in contrast, TFvelo correctly captures the dynamic, with expression increasing consistently from V-SVZ cells (in green). For the NTRK2 gene, TFvelo captures such dynamics correctly, while Multivelo misses the decreasing process at the beginning. On the GRIN2B gene, both TFvelo and Multivelo detect the same dynamics, with expression increasing from the beginning to the terminal stage. These results suggest that by extracting features from multiple TFs, TFvelo can achieve a better fitting for the dynamic of individual gene than Multivelo, without using ATAC-seq. Perhaps the high sparse of ATAC-seq data[52] could lead to mixing of cells from different types and become a challenge for phase portrait fitting. As shown in **Fig. 5c,** TFvelo also provides 3D phase portrait plotting, by combining the spliced and unspliced counts with the learned representation of TFs. The TFvelo's 3D phase portrait can clearly show the correct dynamics.

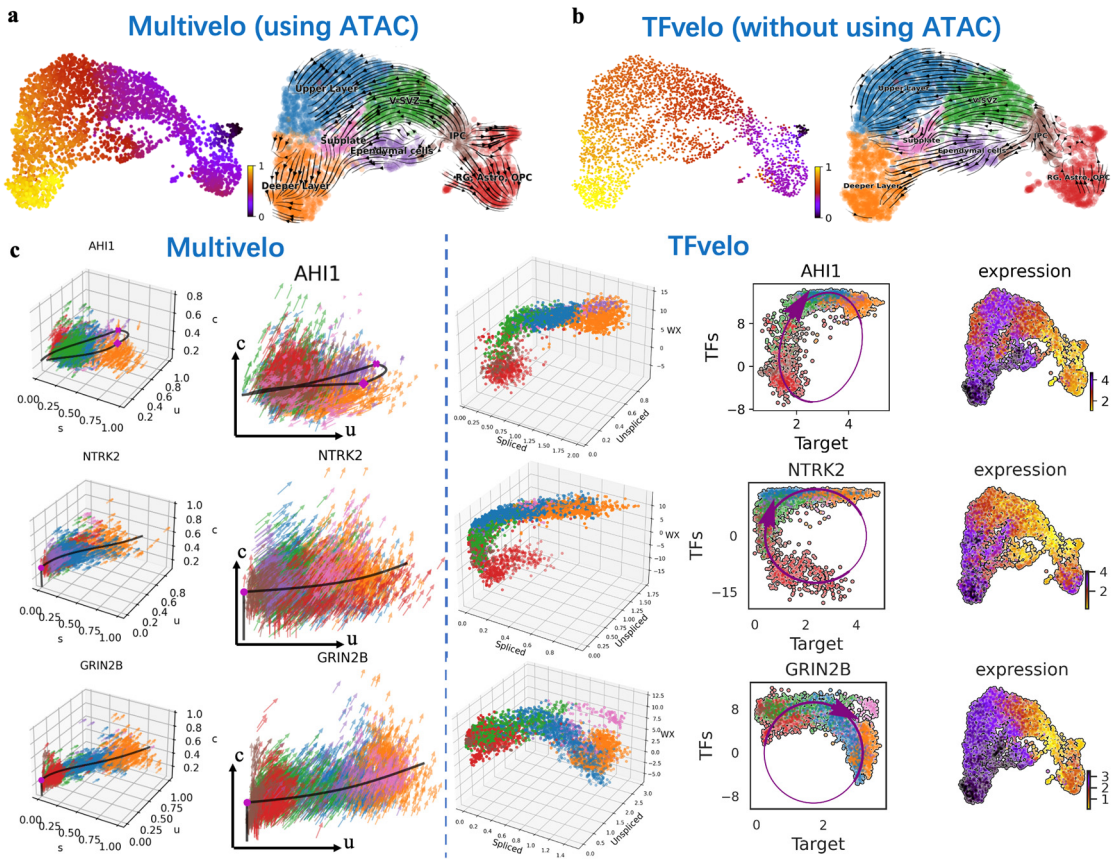

Figure 5. Results of TFvelo on 10x multi-omics embryonic mouse brain dataset. (a) Pseudo-time and trajectory inferenced by Multivelo projected into a UMAP-based embedding. (b) Pseudo-time and trajectory inferenced by TFvelo projected into a UMAP-based embedding. (c) The comparison between Multivelo and TFvelo on three example genes, which are AHI1, NTRK2 and GRIN2B, respectively. For Multivelo plot, c means the chromatin accessibility in ATAC-seq. For TFvelo the 3D phase portrait is obtained by combining the learned representation of TFs (*WX*) with the spliced and unspliced abundance.

TFvelo can predict the cell fate on dataset without splicing information.

Next, TFvelo was applied to another single-cell RNA-seq dataset comprising 1,529 cells obtained from 88 human preimplantation embryos ranging from embryonic day 3 to 7[53]. Since the raw sequencing file is not provided on the online dataset server (see **Data Availability Statement**), those RNA velocity methods relying on the spliced/unspliced information are not feasible. By contrast, TFvelo still successfully identifies the pseudo-time and developmental trajectory of the cells, as depicted in **Fig. 6a** and **Fig. 6b**. Additionally, dynamic models successfully fit the expression patterns of target genes, which are illustrated in **Fig. 6d** as examples. In details, the dynamics predicted on PPP1R14A reveals a clockwise curve on TFs-target plot, and finds the changing point between the increasing and decreasing of expression level at day 5 post-fertilization. Consistent with the TFvelo results, it has been reported that the expression

of PPP1R14A can be detected with high dynamics that it increases at the beginning and declines throughout the development in the early stage of zebrafish embryos[54]. TFvelo finds that the expression of RGS2 is the highest at the beginning, and decreases with the pseudo-time, which can be supported by the early findings that RGS2 plays a critical role in early embryo development[55].

Apart from scRNA-seq, *In Situ* Hybridization (ISH) techniques can also detect RNA abundance at single-cell resolution. However, the splicing information is not provided in the ISH-based datasets, which prevents the application of existing RNA velocity models requiring the splicing input. To show the capability of TFvelo on these data, we then perform TFvelo modelling on a dataset obtained by Multiplexed Error Robust Fluorescence *In Situ* Hybridization (MERFISH)[28,56-58], which is a spatial transcriptomics method based on ISH. On a cultured U-2 OS MERFISH dataset[28], previous studies have identified distinct cell cycle states based on marker genes and GO term analysis[28,59] . They applied scVelo to this dataset, where nuclear and cytoplasmic counts mimic unspliced and spliced transcripts[28,60]. As shown in **Fig. 6e**, without using the nuclear and cytoplasmic counts, which is not always provided in single-cell datasets, TFvelo can also detect the cyclic dynamics from the pseudo-time on the MERFISH dataset. **Fig. 6f** shows genes that are best fitted by TFvelo.

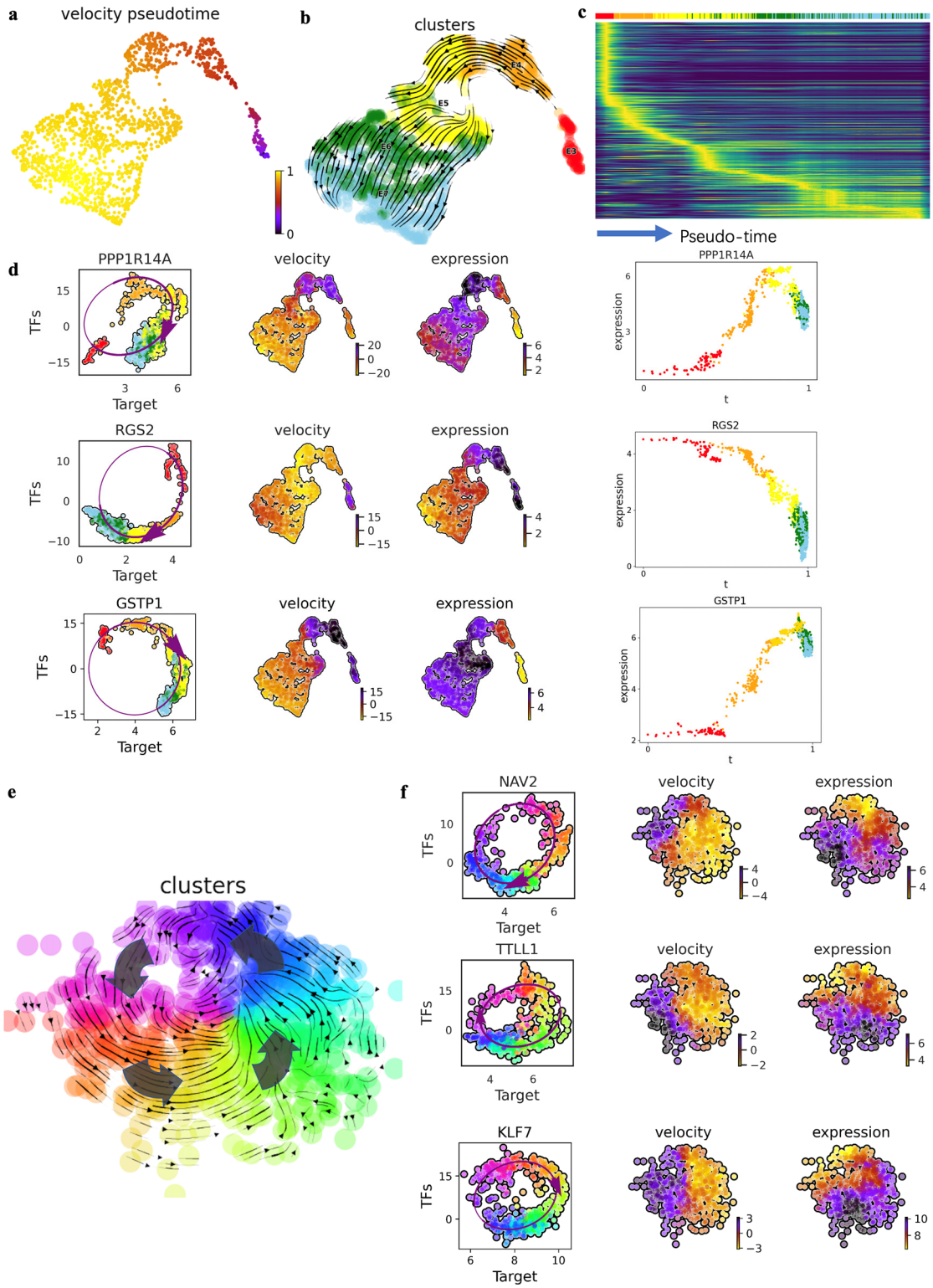

Figure 6. Results of TFvelo on dataset without splicing information. (a-d) Results on human preimplantation embryos dataset. (a) Pseudo-time inferenced by TFvelo projected into a UMAP-based embedding. (b) The streamplot of UMAP. (c) The heatmap which shows the dynamics of gene expression resolved along pseudo-time in the top 300 likelihood-ranked genes. (d) The constructed dynamic models on three example genes with high likelihoods, which are PPP1R14A, RGS2 and GSTP1, respectively. From the left to the right within each row, the three subfigures show phase

portrait fitting, distribution of velocity on UMAP, distribution of expression on UMAP, and the dynamics of expression resolved along with pseudo-time, respectively. (e-f) Results on MERFISH dataset. (e) The stream plot on UMAP. (f) The constructed dynamic models on three example genes with high likelihoods, which are NAV2, TTLL1 and KLF7, respectively. From the left to the right within each row, the three subfigures show phase portrait fitting, distribution of velocity on UMAP, and distribution of expression on UMAP, respectively.

Discussion

The recent development in RNA velocity approaches provide new insights for temporal analysis of single cell data. However, the existing methods often fails to fit the cell dynamics well in the unspliced/spliced space, which is partially because of the insufficient signal and high sparsity and noise. Motivated by the insight that the phase delay between TFs and target can also provide temporal information, we propose TFvelo to estimate the gene dynamics based on TFs abundance. Different from previous approaches which require the splicing information from the data, TFvelo models the dynamics of a target gene with the expression level of TFs and the target gene itself. In the computation framework, a generalized EM algorithm is adopted, so that the latent-time, the weight of TFs and those learnable parameters in the dynamic function can be updated alternately in each iteration.

Experiments on a synthetic dataset validate that TFvelo could detect the underlying dynamics from the data. Results on various scRNA-seq datasets, a MERFISH dataset and a 10x multi-omics dataset further demonstrate that TFvelo can fit the gene dynamics well, showing a desired clockwise curve on the phase portrait between the TFs representation and the target. Furthermore, TFvelo can be used to infer the pseudo time, cell trajectory and detect key TFs which play important role in the differentiation. In addition, compared with the previous RNA velocity model relying on splicing information, TFvelo can achieve better performance on those scRNA-seq datasets, and be flexibly applied to more categories of datasets without splicing information.

In the future, more complex models may be explored to replace the current linear model in TFvelo for estimating the weight of each TFs. The employed sine function for describing expression dynamics could also be replaced by other functional forms flexibly. In addition, those recently proposed ideas for improving unspliced/spliced-based RNA velocity models can also be adopted in the further development of TFvelo, including stochastics modeling with Bayesian inference[14], multi-omics integration[22] and universe time inference[12].

Methods

Data preprocessing.

We utilize the data preparation procedure with the default setting in scVelo [9], where the difference is that TFvelo is applied to the total mRNA counts, which is the sum of unspliced and spliced counts. Additionally, after filtering out those genes that can be detected from fewer than 2% of cells, and selecting the top 2,000 highly variable genes (HVGs), we normalize the expression profile of these HVGs by the total count in each cell. A nearest-neighbor graph (with 30 neighbors by default) was calculated based on Euclidean distances in principal component analysis space (with 30 principal components by default) on log-transformed spliced counts. After that, first-order and second-order moments (means and uncentered variances) are computed for each cell across its nearest neighbors. These steps are implemented with scv.pp.filter_and_normalize() and scv.pp.moments().

Additionally, to find potential transcriptional relationship within the selected 2,000 highly variable genes, we refer to the TF-target pairs annotated in ENCODE TF-target dataset[36] and ChEA TF-target dataset[61]. If the regulatory relationship between a TF-target pair is labeled in at least one of these two datasets, the TF will be included in the involved TFs set when modeling the dynamic of the target gene.

The computational framework of TFvelo

Given a gene g, TFvelo assumes that the RNA velocity $\frac{dy_g(t)}{dt}$ is determined by the expression level of involved TFs $\boldsymbol{X_g}$ and the target gene itself y_g, which is $\frac{dy_g(t)}{dt} = h\left(\boldsymbol{X_g}(t), y_g(t); \Psi_g\right)$. Using a top-down strategy [12], TFvelo directly designs a profile function of target gene's expression level to relax the gene dynamics to more flexible profiles, that is $y_g(t) = f\left(t; \Phi_g\right)$. Ψ_g and Φ_g are two sets of gene-specific, time-invariant parameters, which control the influence of TFs on the target gene, and the shape of target gene's phase portraits, respectively. Our findings and early studies [37] have shown that it is feasible to infer the regulation relationship according to the learned parameter in linear regression models based on expression data. Additionally, linear models always have high interpretability, and rarely suffer from over-fitting. As a result, to show the capability of modeling RNA velocity based on gene regulatory relationship, we simply adopt a linear model as $h\left(\boldsymbol{X_g}(t), y_g(t); \Psi_g\right)$, which can map the expression levels of multiple TFs $X_g \in R^{n_{TF}}$ from n_{TF}-dimensional space to 1-dimensional representation $W_g X_g$ with a weight vector W_g, where n_{TF} represents the number of involved TFs. As a result, the dynamic equation between TFs and the target gene g can be written as

$$\frac{dy_g(t)}{dt} = h\left(\boldsymbol{X_g}(t), y_g(t); \Psi_g\right) = \boldsymbol{W_g}\boldsymbol{X_g}(t) - \gamma_g y_g(t)\,, \tag{4}$$

where $t \in [0,1)$ is the latent time assigned to each cell, γ_g is the degradation rate.

Besides, The profile function of $y_g(t)$ can be chosen flexibly from those second-order differentiable functions [12]. For simplification, $y_g(t)$ is designed with a sine function in our implementation, which is high-order differentiable and suitable for capture the curves on phase portrait. In addition, different with those models which assume the gene expression should follow a pattern of initial improvement followed by a decrease (or part of the whole process), TFvelo is more flexible and can also model gene dynamics where expression initially decreases and later increases with the sine function.

$$y_g(t) = f(t; \Phi_g) = \alpha_g \, sin(\omega_g t + \theta_g) + \beta_g, \tag{5}$$

where $\alpha_g, \beta_g, \theta_g$ are gene-specific parameters to be learned. ω_g is fixed as 2π, so that the $y_g(t)$ is unimodal within $t \in [0,1)$, which follows the common assumption shared by most current approaches. By employing the sin function, TFvelo can model the dynamics of each gene without defining a switching time point between the of increasing and decreasing periods [8 9 14 18]. To optimize the parameters in TFvelo, a generalized EM [40,41] algorithm is adopted, as discussed in the following.

Optimization of generalized EM algorithm

To simplify the mathematical representation, here we denote the $\boldsymbol{W_g}, \boldsymbol{X_g}, y_g, \alpha_g, \beta_g, \theta_g, \gamma_g$ and ω_g as $\boldsymbol{W}, \boldsymbol{X}, y, \alpha, \beta, \theta, \gamma$ and ω, respectively. As a result, the equation (5) and (4) can be written as

$$y(t) = \alpha \sin(2\pi t + \theta) + \beta, \tag{6}$$

$$\frac{dy(t)}{dt} = \boldsymbol{WX}(t) - \gamma y(t). \tag{7}$$

From the dynamics model in equation (6) and (7), we can derive that,

$$\boldsymbol{WX}(t) = \alpha\sqrt{4\pi^2 + \gamma^2}\, sin(2\pi t + \theta + \phi) + \beta\gamma, \phi = arctan\left(\frac{2\pi}{\gamma}\right), \tag{8}$$

For modeling a gene, suppose observations $\boldsymbol{X_c^{obs}}$ and y_c^{obs} be the normalized expression levels of TFs and the target gene within a cell c, s_c^{obs} be the state space representation of the cell c, and $\hat{s}(t_c)$ be the modeled state at time t_c, we have $s_c^{obs} = \left[\boldsymbol{WX_c^{obs}}, y_c^{obs}\right]$ and $\hat{s}(t_c) = [\boldsymbol{WX}(t_c), y(t_c)]$. Aiming at finding the phase trajectory $\hat{s}(t)$ that best fits the observations for all cells, we define the loss function as:

$$L = \sum_c ||s_c^{obs} - \hat{s}(t_c)||^2 = \sum_c (\boldsymbol{WX_c^{obs}} - \boldsymbol{WX}(t_c))^2 + (y_c^{obs} - y(t_c))^2, \tag{9}$$

The residuals of the observations are defined as $e_c = sign(y_c^{obs} - y(t_c))||s_c^{obs} - \hat{s}(t_c)||^2$, which is assumed to follow a normal distribution $e_c \sim N(0, \sigma^2)$, where the gene-specific σ is constant across cells, and the observations are independent and identically distributed. Then we can arrive at the likelihood function,

$$\mathcal{L}(\boldsymbol{W}, \alpha, \beta, \theta, \gamma) = \frac{1}{\sqrt{2\pi}\sigma} * \exp\left(-\frac{1}{2\sigma^2}\sum_c ||s_c^{obs}(\boldsymbol{W}) - \hat{s}_{t_c}(\boldsymbol{W}, \alpha, \beta, \theta, \gamma)||^2\right), \tag{10}$$

Where $\hat{s}_{t_c}(\boldsymbol{W},\alpha,\beta,\theta,\gamma)$ represents $\hat{s}(t_c;\boldsymbol{W},\alpha,\beta,\theta,\gamma)$. Finally, the optimization algorithm aims to minimize the negative log-likelihood function:

$$l(\boldsymbol{W},\alpha,\beta,\theta,\gamma) = -\log\left(\frac{1}{\sqrt{2\pi}\sigma}\right) + \frac{1}{2\sigma^2}\sum_c ||s_c^{obs}(\boldsymbol{W}) - \hat{s}_{t_c}(\boldsymbol{W},\alpha,\beta,\theta,\gamma)||^2, \quad (11)$$

In standard EM algorithms, the E-step computes the expected value of likelihood function given the observed data and the current estimated parameters to update the latent variables, and the M-step consists of maximizing that expectation computed in E step by optimizing the parameters. While under some circumstances, there is an intractable problem in M step, which could be addressed by generalized EM algorithms. Expectation conditional maximization is one form of generalized EM algorithms, which makes multiple constraint optimizations within each M step [40]. In detail, the parameters can be separated into more subsets, and the M step consists of multiple steps as well, each of which optimizes one subset of parameters with the reminder fixed [41].

In TFvelo, all learnable parameters can be divided into three groups, which are cell-specific latent time $t \in R^{n_{cell}}$, weight of each TF $\mathbf{W} \in R^{n_{TF}}$ and scalars $[\alpha,\beta,\theta,\ \gamma]$ respectively, where n_{cell} and n_{TF} represent the number of cells and the number of involved TFs. Generalized EM algorithm is adopted so that the three group of parameters will be updated alternately to minimize the loss function in each iteration:

a) Assign t within [0,1) for each cell by grid search. For each cell, on the phase plot, the closest point located on the curve described by the dynamic model is defined as the target point. The step b) and c) aim to minimize the average distance between cells and their corresponding target points.
b) Update W by linear regression with bounds on these weights to minimize the loss function. Trust region reflective algorithm [62], which is an interior-point-like method is adopted to solve this linear least-squares problem with inequality constraint. In our implementation, the weights are bounded within (-20, 20) by default.
c) Update $[\alpha,\beta,\theta,\ \gamma]$ with constraints of $\alpha\in(0,\ \infty)$, $\theta\in(-\pi,\ \pi)$ and $\gamma\in(0,\ \infty)$ to minimize the loss function.

By iteratively running the three steps, parameters of TFvelo for each target gene can be optimized. Furthermore, multiple downstream analysis could be conducted by combining the learned dynamics of all target genes.

Initialization of the generalized EM algorithm.

Since EM algorithms could be trapped in local minimum, parameters are initialized in the following steps. Firstly, those cells in which expression of target gene is 0 are filtered out. Then X, y are normalized by $\boldsymbol{X} = \boldsymbol{X}/var(\boldsymbol{X})$, $y = y/var(y)$, where $var(\cdot)$ represents the standard deviation function. The weights $\boldsymbol{W}$ is initialized with the value of spearman correlation of each TF-target pair. For parameters α,β and γ ,

according to the steady-state assumption that $\dot{y}|_{y=max\,(y)} = 0$, γ can be initialized by $\gamma = \frac{\boldsymbol{W}\mathbf{X}}{y}|_{y \to y_{max}}$. At the points of maximal and minimal y value, we have $y_{max} = \alpha + \beta$ and $y_{min} = -\alpha + \beta$. As a result, α and β can be initialized by $\alpha = \frac{y_{max} - y_{min}}{2}$ and $\beta = \frac{y_{max} + y_{min}}{2}$, respectively. These assumptions are only used for initialization and in the following optimization process, all parameters will be updated iteratively. The hyper-parameter ω is set as 2π and parameter θ isintialized with various values, so that the generalized EM algorithm will run at different start points. After that, the model with the lowest loss is finally selected.

Inference of Pseudo-time

After constructing the dynamic model for each gene, TFvelo will infer a gene-agnostic pseudo-time for each cell based on the combination of RNA velocities of all genes. For this purpose, we first compute the cosine similarities between velocities and potential cell state transitions to get the transition matrix. Then the end points and root cells are obtained as stationary states of the velocity-inferred transition matrix and its transposed, respectively. After inferring the root cells' location on the embedding space, velocity pseudo-time, which measures the average number of steps it takes to reach a cell after start walking from root cells, can be computed. The strategy of calculating pseudo-time is the similar with that in scVelo [9]. The different is that in scVelo, the transition matrix is obtained based on the abundance and velocity of spliced mRNA, while in TFvelo that is based on the abundance and velocity of total mRNA.

Velocity streams on 2D embedding space

To illustrate cell transitions, we create stream plots in a 2D space using UMAP visualization as the default. To this end, we select genes whose loss is low and gene-specific time aligns with the pseudotime to construct velocity streams.

For the single cell datasets, we first select genes with modeling error in the bottom 50%. Since sine functions exhibit periodicity, we need to determine the order of cells instead of using latent time directly. We achieve this by analyzing the histogram of latent time. If there are several consecutive blank bins in the cell distribution of latent time, we set the minimum value of the next non-blank bin as the initial state (normalized latent time = 0). Conversely, the maximum value of the last non-blank bin will be set as the final state (normalized latent time = 1). The normalized latent time of all other cells will be mapped within the range of 0 to 1. Subsequently, we select genes where the normalized latent time aligns with the pseudotime based on the Spearman correlation coefficient between them.

For the MERFISH dataset of human osteosarcoma (U-2 OS) cells, since our focus is on analyzing the cell cycle process, we choose genes that exhibit periodic dynamics. To achieve this, we analyze the histogram of latent time and only select genes with no non-blank bins, indicating that their dynamics cover the entire periodic curve on the phase portrait. We then perform clustering within the selected genes, choosing the largest gene clusters as the best-fitted genes, by which the velocity graph following velocity embedding stream are generated in the same strategy as that in scvelo.

Metrics for evaluating in phase portrait.

We propose three metrics for phase portrait fitting.

(1) The intra-class distance on phase portrait, which measures the normalized distance between cells within the same type on the phase portrait. This reflects whether cells within the same type gather on the phase portrait, which is the lower the better. On unspliced/spliced based methods, the intra-class distance is defined as $Dist = \sum_k \sum_{j \in type_k} [(\frac{u_j - u_c^k}{std(u)})^2 + (\frac{s_j - s_c^k}{std(s)})^2]$, where (u_c^k, s_c^k) means the center of cell type k, std(.) means the standard variance and j means the index of a cell. For TFvelo, the distance can be defined by substituting u with WX and s with y.

(2) The inter-class distance on phase portrait, which measures the normalized distance between the distribution centers of different cell types on the phase portrait, which is defined as $Dist = \sum_{k1 \neq k2} [(\frac{u_c^{k1} - u_c^{k2}}{std(u)})^2 + (\frac{s_c^{k1} - s_c^{k2}}{std(s)})^2]$. This reflects whether cells from different types are separated well on the phase portrait, which is the higher the better.

(3) The fitting error on phase portrait, which measures the normalized distance between each cell to the constructed model on the phase portrait. This reflects the fitting accuracy and calculated in the following way. On the phase portrait of each selected gene, calculate the normalized mean square error of the distance between each cell to the inferred model curve. For the TFvelo data, $Err = \sum_{j=1}^{N} [(\frac{WX_j - WX(t_j)}{std(WX)})^2 + (\frac{y_j - y(t_j)}{std(y)})^2]$, where j means the index of a cell , t_j means the latent time modeled for cell j and N is the total number of cells. $\boldsymbol{WX_j}$ and y_j refer to the location of cell on the phase portrait. $\boldsymbol{WX}(t_j)$ and $y(t_j)$ refers to the model given by TFvelo. Similarly, the error for un/spliced data-based methods is defined as $Err = \sum_{j=1}^{N} [(\frac{u_j - u(t_j)}{std(u)})^2 + (\frac{s_j - s(t_j)}{std(s)})^2]$.

GO term and KEGG pathway enrichment analysis

To perform the GO term and KEGG pathway enrichment analysis, we utilized the

"gseapy.enrichr()" function in Python package "gseapy" with using Fisher's exact test by default. For each dataset, the background gene list consists of all genes within the original dataset before preprocessing.

Weights Normalization and TFs selection

Considering that the abundance of different TFs could vary a lot, the quantitative comparison between the weights of TFs is conducted after normalizing them. For each TF on modeling a target, we multiply the mean expression level by the learned weights to get the average influence of the TF to the target gene. For instance, the average influence of TF i is $w_i * \bar{x}_i$. Then the normalized weights are defined as: $\widetilde{w}_i = \frac{w_i * \bar{x}_i}{max_i(|w_i * \bar{x}_i|)}$. The TFs with high weights are select according to these normalized weights with default threshold of 0.5.

Data Availability Statement

The pancreatic endocrinogenesis dataset is available from NCBI GEO under accession ID GSE132188. It comprises the single-cell RNA-seq (10X) data of 27,998 genes of 3,696 pancreatic epithelial and Ngn3-Venus fusion cells sampled from mouse embryonic day 15.5. Data could be acquired from scv.datasets.pancreas().

The gastrulation erythroid dataset, which is selected from the transcriptional profiles of mouse embryos [46], provides expressions of 53,801 genes of 9,815 cells. This dataset is incorporated by scv.datasets.gastrulation_erythroid().

10x embryonic mouse brain dataset can be accessed at the 10x website at https://www.10xgenomics.com/resources/datasets/fresh-embryonic-e-18-mouse-brain-5-k-1-standard-1-0-0.

Human preimplantation embryos dataset is a single-cell RNA-seq dataset of 1,529 cells obtained from 88 human preimplantation embryos ranging from embryonic day 3 to 7. Data were downloaded with the accession number of E-MTAB-3929 from EMBL-EBI [53]. In this dataset, only the RNA abundance is provided. As a result, those RNA velocity methods relying on the spliced/unspliced are not available.

The MERFISH of dataset, consisting of the expression of 10,050 genes in 1,368 human osteosarcoma cells from 3 batches (replicates), is available at https://www.pnas.org/doi/10.1073/pnas.1912459116#supplementary-materials [28]. The cell embedding are from Veloviz [60].

Code Availability Statement

TFvelo is implemented in Python, based on the scVelo package [9]. The source code can be downloaded from the GitHub repository, https://github.com/xiaoyeye/TFvelo.

Acknowledgement

This work was supported by the National Natural Science Foundation of China (No. 61725302, 62073219 and 62103262), Shanghai Pujiang Program (No. 21PJ1407700), and the Science and Technology Commission of Shanghai Municipality (22511104100).

References

1 Saliba, A.-E., Westermann, A. J., Gorski, S. A. & Vogel, J. Single-cell RNA-seq: advances and future challenges. *Nucleic acids research* **42**, 8845-8860 (2014).

2 Chen, G., Ning, B. & Shi, T. Single-cell RNA-seq technologies and related computational data analysis. *Frontiers in genetics*, 317 (2019).

3 Kiselev, V. Y., Andrews, T. S. & Hemberg, M. Challenges in unsupervised clustering of single-cell RNA-seq data. *Nature Reviews Genetics* **20**, 273-282 (2019).

4 Wolf, F. A. *et al.* PAGA: graph abstraction reconciles clustering with trajectory inference through a topology preserving map of single cells. *Genome biology* **20**, 1-9 (2019).

5 Qiu, X. *et al.* Reversed graph embedding resolves complex single-cell trajectories. *Nature methods* **14**, 979-982 (2017).

6 Street, K. *et al.* Slingshot: cell lineage and pseudotime inference for single-cell transcriptomics. *BMC genomics* **19**, 1-16 (2018).

7 Setty, M. *et al.* Characterization of cell fate probabilities in single-cell data with Palantir. *Nature biotechnology* **37**, 451-460 (2019).

8 La Manno, G. *et al.* RNA velocity of single cells. *Nature* **560**, 494-498 (2018).

9 Bergen, V., Lange, M., Peidli, S., Wolf, F. A. & Theis, F. J. Generalizing RNA velocity to transient cell states through dynamical modeling. *Nature biotechnology* **38**, 1408-1414 (2020).

10 Qiao, C. & Huang, Y. Representation learning of RNA velocity reveals robust cell transitions. *Proceedings of the National Academy of Sciences* **118**, e2105859118 (2021).

11 Riba, A. *et al.* Cell cycle gene regulation dynamics revealed by RNA velocity and deep-learning. *Nature communications* **13**, 1-13 (2022).

12 Gao, M., Qiao, C. & Huang, Y. UniTVelo: temporally unified RNA velocity reinforces single-cell trajectory inference. *Nature Communications* **13**, 6586 (2022).

13 Gayoso, A. *et al.* Deep generative modeling of transcriptional dynamics for RNA velocity analysis in single cells. *bioRxiv*, 2022.2008. 2012.503709 (2022).

14 Qin, Q., Bingham, E., La Manno, G., Langenau, D. M. & Pinello, L. Pyro-Velocity: Probabilistic RNA Velocity inference from single-cell data. *bioRxiv* (2022).

15 Gu, Y., Blaauw, D. & Welch, J. D. Bayesian inference of rna velocity from multi-lineage

765 single-cell data. *bioRxiv* (2022).
766 16 Farrell, S., Mani, M. & Goyal, S. Inferring single-cell dynamics with structured dynamical
767 representations of RNA velocity. *bioRxiv*, 2022.2008. 2022.504858 (2022).
768 17 Li, S. *et al.* A relay velocity model infers cell-dependent RNA velocity. *Nature*
769 *biotechnology*, 1-10 (2023).
770 18 Qiu, X. *et al.* Mapping transcriptomic vector fields of single cells. *Cell* **185**, 690-711. e645
771 (2022).
772 19 Cao, J., Zhou, W., Steemers, F., Trapnell, C. & Shendure, J. Sci-fate characterizes the
773 dynamics of gene expression in single cells. *Nature biotechnology* **38**, 980-988 (2020).
774 20 Ma, A., McDermaid, A., Xu, J., Chang, Y. & Ma, Q. Integrative methods and practical
775 challenges for single-cell multi-omics. *Trends in biotechnology* **38**, 1007-1022 (2020).
776 21 Subramanian, I., Verma, S., Kumar, S., Jere, A. & Anamika, K. Multi-omics data
777 integration, interpretation, and its application. *Bioinformatics and biology insights* **14**,
778 1177932219899051 (2020).
779 22 Gorin, G., Svensson, V. & Pachter, L. Protein velocity and acceleration from single-cell
780 multiomics experiments. *Genome biology* **21**, 1-6 (2020).
781 23 Li, C., Virgilio, M., Collins, K. L. & Welch, J. D. in *International Conference on Research in*
782 *Computational Molecular Biology.* 297-299 (Springer).
783 24 Liu, R., Pisco, A. O., Braun, E., Linnarsson, S. & Zou, J. Dynamical Systems Model of RNA
784 Velocity Improves Inference of Single-cell Trajectory, Pseudo-time and Gene Regulation.
785 *Journal of Molecular Biology*, 167606 (2022).
786 25 Bergen, V., Soldatov, R. A., Kharchenko, P. V. & Theis, F. J. RNA velocity—current
787 challenges and future perspectives. *Molecular systems biology* **17**, e10282 (2021).
788 26 Gorin, G., Fang, M., Chari, T. & Pachter, L. RNA velocity unraveled. *PLOS Computational*
789 *Biology* **18**, e1010492 (2022).
790 27 Soneson, C., Srivastava, A., Patro, R. & Stadler, M. B. Preprocessing choices affect RNA
791 velocity results for droplet scRNA-seq data. *PLoS computational biology* **17**, e1008585
792 (2021).
793 28 Xia, C., Fan, J., Emanuel, G., Hao, J. & Zhuang, X. Spatial transcriptome profiling by
794 MERFISH reveals subcellular RNA compartmentalization and cell cycle-dependent gene
795 expression. *Proceedings of the National Academy of Sciences* **116**, 19490-19499 (2019).
796 29 Kim, J., T. Jakobsen, S., Natarajan, K. N. & Won, K.-J. TENET: gene network
797 reconstruction using transfer entropy reveals key regulatory factors from single cell
798 transcriptomic data. *Nucleic acids research* **49**, e1-e1 (2021).
799 30 Qiu, X. *et al.* Inferring causal gene regulatory networks from coupled single-cell
800 expression dynamics using scribe. *Cell systems* **10**, 265-274. e211 (2020).
801 31 Aibar, S. *et al.* SCENIC: single-cell regulatory network inference and clustering. *Nature*
802 *methods* **14**, 1083-1086 (2017).
803 32 Matsumoto, H. *et al.* SCODE: an efficient regulatory network inference algorithm from
804 single-cell RNA-Seq during differentiation. *Bioinformatics* **33**, 2314-2321 (2017).
805 33 Wang, L. *et al.* Dictys: dynamic gene regulatory network dissects developmental
806 continuum with single-cell multiomics. *Nature Methods*, 1-11 (2023).
807 34 Yuan, Y. & Bar-Joseph, Z. Deep learning of gene relationships from single cell time-
808 course expression data. *Briefings in bioinformatics* **22** (2021).

809 35 Lambert, S. A. *et al.* The human transcription factors. *Cell* **172**, 650-665 (2018).
810 36 Feingold, E. *et al.* The ENCODE (ENCyclopedia of DNA elements) project. *Science* **306**,
811 636-640 (2004).
812 37 Tran, A., Yang, P., Yang, J. Y. & Ormerod, J. T. scREMOTE: Using multimodal single cell
813 data to predict regulatory gene relationships and to build a computational cell
814 reprogramming model. *NAR Genomics and Bioinformatics* **4**, lqac023 (2022).
815 38 Song, Q., Ruffalo, M. & Bar-Joseph, Z. Using single cell atlas data to reconstruct
816 regulatory networks. *Nucleic Acids Research* **51**, e38-e38 (2023).
817 39 Liu, Y.-Y., Slotine, J.-J. & Barabási, A.-L. Controllability of complex networks. *nature* **473**,
818 167-173 (2011).
819 40 Meng, X.-L. & Rubin, D. B. Maximum likelihood estimation via the ECM algorithm: A
820 general framework. *Biometrika* **80**, 267-278 (1993).
821 41 Bishop, C. M. & Nasrabadi, N. M. *Pattern recognition and machine learning*. Vol. 4
822 (Springer, 2006).
823 42 Kim, D., Zhang, L., Dzau, V. & Pratt, R. H19, a developmentally regulated gene, is
824 reexpressed in rat vascular smooth muscle cells after injury. *The Journal of clinical*
825 *investigation* **93**, 355-360 (1994).
826 43 Carmo-Fonseca, M. & Kirchhausen, T. The timing of pre-mRNA splicing visualized in
827 real-time. *Nucleus* **5**, 11-14 (2014).
828 44 Elhanani, O. *et al.* REST inhibits direct reprogramming of pancreatic exocrine to
829 endocrine cells by preventing PDX1-mediated activation of endocrine genes. *Cell*
830 *Reports* **31** (2020).
831 45 Rovira, M. *et al.* REST is a major negative regulator of endocrine differentiation during
832 pancreas organogenesis. *Genes & development* **35**, 1229-1242 (2021).
833 46 Pijuan-Sala, B. *et al.* A single-cell molecular map of mouse gastrulation and early
834 organogenesis. *Nature* **566**, 490-495 (2019).
835 47 Guyot, R., Vincent, S., Bertin, J., Samarut, J. & Ravel-Chapuis, P. The transforming acidic
836 coiled coil (TACC1) protein modulates the transcriptional activity of the nuclear
837 receptors TR and RAR. *BMC Molecular Biology* **11**, 1-13 (2010).
838 48 Gutiérrez, L., Caballero, N., Fernández-Calleja, L., Karkoulia, E. & Strouboulis, J.
839 Regulation of GATA1 levels in erythropoiesis. *IUBMB life* **72**, 89-105 (2020).
840 49 Nanaa, A. *et al.* Clinical and biological characteristics and prognostic impact of somatic
841 GATA2 mutations in myeloid malignancies: a single institution experience. *Blood cancer*
842 *journal* **11**, 122 (2021).
843 50 Wadman, I. A. *et al.* The LIM-only protein Lmo2 is a bridging molecule assembling an
844 erythroid, DNA-binding complex which includes the TAL1, E47, GATA-1 and Ldb1/NLI
845 proteins. *The EMBO journal* **16**, 3145-3157 (1997).
846 51 Buenrostro, J. D., Giresi, P. G., Zaba, L. C., Chang, H. Y. & Greenleaf, W. J. Transposition
847 of native chromatin for fast and sensitive epigenomic profiling of open chromatin, DNA-
848 binding proteins and nucleosome position. *Nature methods* **10**, 1213-1218 (2013).
849 52 Ji, Z., Zhou, W., Hou, W. & Ji, H. Single-cell ATAC-seq signal extraction and
850 enhancement with SCATE. *Genome biology* **21**, 1-36 (2020).
851 53 Chu, L.-F. *et al.* Single-cell RNA-seq reveals novel regulators of human embryonic stem
852 cell differentiation to definitive endoderm. *Genome biology* **17**, 1-20 (2016).

853 54 Lang, I. *et al.* The evolution of duplicated genes of the Cpi-17/Phi-1 (ppp1r14) family of
854 protein phosphatase 1 inhibitors in teleosts. *International Journal of Molecular Sciences*
855 **21**, 5709 (2020).
856 55 Zhu, Y. *et al.* Knockdown of regulator of G-protein signalling 2 (Rgs2) leads to abnormal
857 early mouse embryo development in vitro. *Reproduction, Fertility and Development* **27**,
858 557-566 (2015).
859 56 Moffitt, J. R. & Zhuang, X. RNA imaging with multiplexed error-robust fluorescence in
860 situ hybridization (MERFISH). *Methods in enzymology* **572**, 1-49 (2016).
861 57 Moffitt, J. R. *et al.* High-throughput single-cell gene-expression profiling with
862 multiplexed error-robust fluorescence in situ hybridization. *Proceedings of the National*
863 *Academy of Sciences* **113**, 11046-11051 (2016).
864 58 Chen, K. H., Boettiger, A. N., Moffitt, J. R., Wang, S. & Zhuang, X. Spatially resolved,
865 highly multiplexed RNA profiling in single cells. *Science* **348** (2015).
866 59 Li, J., Chen, S., Pan, X., Yuan, Y. & Shen, H.-B. Cell clustering for spatial transcriptomics
867 data with graph neural networks. *Nature Computational Science* **2**, 399-408 (2022).
868 60 Atta, L., Sahoo, A. & Fan, J. VeloViz: RNA velocity-informed embeddings for visualizing
869 cellular trajectories. *Bioinformatics* **38**, 391-396 (2022).
870 61 Lachmann, A. *et al.* ChEA: transcription factor regulation inferred from integrating
871 genome-wide ChIP-X experiments. *Bioinformatics* **26**, 2438-2444 (2010).
872 62 Branch, M. A., Coleman, T. F. & Li, Y. A subspace, interior, and conjugate gradient
873 method for large-scale bound-constrained minimization problems. *SIAM Journal on*
874 *Scientific Computing* **21**, 1-23 (1999).
875
876
877